All-Vacuum-Deposited Stoichiometrically Balanced Inorganic Cesium Lead Halide Perovskite Solar Cells with Stabilized Efficiency Exceeding 11%

*Chien-Yu Chen, Hung-Yu Lin, Kai-Ming Chiang, Wei-Lun Tsai, Yu-Ching Huang, Cheng-Si Tsao, and Hao-Wu Lin**

In this work, vacuum-deposited inorganic cesium lead halide perovskite thin films were developed by co-sublimation of cesium halide and lead halide precursors in high vacuum. To accurately control the stoichiometric ratios of the precursors in the perovskite thin films, the hygroscopic nature of the alkali halides was carefully considered. By integrating vacuum-sublimed hole and electron transport layers, all-vacuum-deposited solar cells were fabricated. The devices with stoichiometrically balanced precursor ratios exhibited significantly better performances than those with nonstoichiometric molar ratios. Power conversion efficiency of 9.4% was achieved with $CsPbI_3$ (band gap 1.72 eV). Mixed halides with a band gap of 1.82 eV further boosted the device power conversion efficiency to 11.8%, contributing also to high open-circuit voltage (1.13 V), small hysteresis, and superior thin-film and device stabilities.

Organometallic halide perovskites have attracted increasing interest due to their intriguing photophysical properties as well as commercial applications in solar cells, indoor energy harvesting devices, and light-emission devices.[1–6] Currently, most research studies on perovskite thin film fabrication focus on solution-processing methods; however, vacuum deposition provides a promising way to obtain halide perovskites, offering great advantages such as good uniformity, high reproducibility, and mature industrial fabrication facilities.[7–10] However, the energy requirements associated with vacuum processing are substantial and could hinder the advantage of the rapid energy payback time of perovskites.[11] Vacuum deposition methods usually involve the sublimation of two kinds of precursors, typically organic and metal halides (mainly, lead halides), in a vacuum chamber. However, the gas-like behavior of organic halides, owing to their small molecular weight, makes the process very difficult to monitor and control; besides, contamination problems are also an issue. To solve this problem and fabricate vacuum-deposited perovskite solar cells with decent efficiencies, researchers have developed sequential vacuum deposition and chemical vapor deposition methods.[8,12–14] Another way to unlock the full potential of vacuum deposition for the fabrication of perovskite films entails the use of precursors without gas-like properties.[15] In this communication, we show that, by replacing organic halides with cesium halides, common vacuum deposition techniques can be applied smoothly to the fabrication of perovskite solar cells. Cesium-based perovskite thin films, $CsPbI_3$ (band gap, E_g, of 1.72 eV), and $CsPbI_2Br$ (E_g = 1.82 eV), with intriguing morphological and photophysical properties were obtained. By combining these films with vacuum-sublimed hole and electron transport layers (HTLs and ETLs), efficient all-vacuum-deposited $CsPbI_3$ and $CsPbI_2Br$ solar cells were made. The best device showed the highest current-density-to-voltage (J–V) sweeping power conversion efficiency (PCE) of 11.8% and similar stabilized PCE up to 11.5%, which exceeded the values observed for the best solution-processed cesium-based perovskite solar cells.[16–18] Furthermore, their high open-circuit voltage (V_{oc}) makes them very suitable as dim-light energy harvesters. High PCE of 26.6% was observed under 1000 lux fluorescent light. High efficiency under both 1 sun and dim-light conditions, and the truly physical vapor behavior of sublimed precursors make cesium-based perovskite a very promising solar active material especially suitable for vacuum deposition fabrication.

In the most widely studied one-step $CH_3NH_3PbI_3$ perovskite preparation methods, thin films are coated from a solution mixture of two precursors—i.e., lead halide (usually PbI_2) and organic halide, CH_3NH_3I (methylammonium iodide, MAI)—in equal stoichiometric molar ratio. However, when the same concept is applied to vacuum codeposition, stoichiometric equality can be hardly achieved, owing to the gas-like nature of MAI even under high vacuum. Instead of employing the two-step solid-state (PbI_2) gas (MAI) reaction method, the use of alternative precursors, i.e., cesium halides, opens up new opportunities for high-vacuum fabrication of perovskite with considerably superior controllability. Cesium halides, e.g., CsF, are commonly used for electron injection layers in vacuum-deposited organic light-emission devices (OLEDs).[19] Nevertheless, in OLED applications, a subnanometer CsF interfacial layer is sufficient for electron injection, and precise thickness is not critical for the device operation.[20,21] Conversely, if cesium halide is used as one of the two precursors in the vacuum codeposition process, an accurate control of the amount deposited on the substrate is a prerequisite for a stoichiometrically balanced deposition. In vacuum deposition, a precise deposition rate is commonly monitored by a quartz crystal microbalance, which

C.-Y. Chen, H.-Y. Lin, K.-M. Chiang, W.-L. Tsai, Prof. H.-W. Lin
Department of Materials Science and Engineering
National Tsing Hua University
Hsinchu 30013, Taiwan
E-mail: hwlin@mx.nthu.edu.tw
Dr. Y.-C. Huang, Dr. C.-S. Tsao
Institute of Nuclear Energy Research
Taoyuan 32546, Taiwan

DOI: 10.1002/adma.201605290

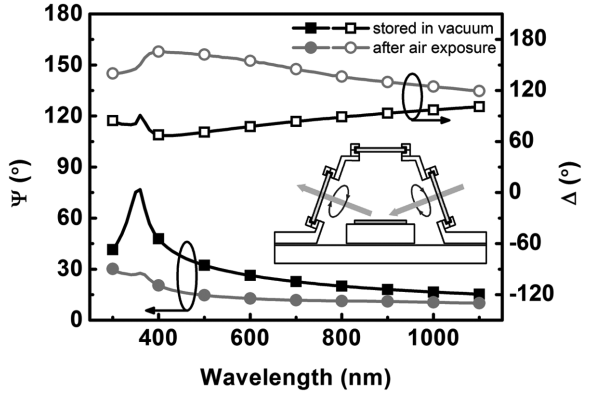

Figure 1. Ellipsometric data of unexposed and air-exposed (3 min) 50 nm thick CsI thin films on silicon substrate. Inset: Schematic diagram of the vacuum chamber setup.

is precalibrated by an ellipsometer. Notably, the hygroscopic nature of cesium halides needs to be carefully considered during the calibration. When exposed to air for only a few minutes, CsI thin films dramatically change from transparent and reflective surface to rough and diffusive appearance. Hence, a custom-made vacuum chamber with observation and measurement windows was utilized to avoid air exposure, as illustrated in the schematic diagram in **Figure 1**. The cesium halide thin films were kept under 10^{-3} torr vacuum throughout the transportation and measurement. Figure 1 shows the ellipsometric data of CsI thin films unexposed and exposed to air for only 3 min. Largely distinct values were found, indicating that the correct calibration of the vacuum-deposited cesium halide thin-film thickness can only be done without exposing the film to air. The fitted thickness of the unexposed film was 50 nm, while the exposed film exhibited a thickness of 23 nm. The results indicated that the thickness of hygroscopic CsI can be easily miscalculated, appearing as low as half of the correct value.

After careful calibration of PbI_2 and CsI, thin films of codeposited PbI_2 and CsI with various molar ratios were fabricated. The films were postannealed at 325 °C to turn their appearance to the dark-brownish perovskite phase.[22] **Figure 2**a shows the absorption spectra of the $CsPbI_3$ thin films. All films exhibited an onset at 720 nm, which is characteristic of $CsPbI_3$ perovskite.[22] The stoichiometrically balanced (PbI_2:CsI = 1:1) $CsPbI_3$ thin film showed the highest absorption. In contrast, perovskite thin films with unbalanced precursor ratios exhibited significantly lower absorptions, indicating that a lower amount of $CsPbI_3$ was formed after thermal annealing. PbI_2-rich thin films showed an absorption plateau at ≈500 nm, corresponding to the PbI_2 band edge absorption. Figure 2b displays the performances of the solar cells utilizing these active layers. The corresponding external quantum efficiency (EQE) spectra are showed in Figure S1 in the Supporting Information. The best $CsPbI_3$ solar cell with 1:1 stoichiometric ratio showed the PCE of 9.4%, with V_{oc} of 0.98 V, short-circuit current density (J_{sc}) of 17.3 mA cm^{-2}, and fill factor (FF) of 0.56, while the PbI_2-rich and CsI-rich $CsPbI_3$ solar cells showed lower J_{SC} and FF values. The best PbI_2:CsI = 1.3:1 solar cell delivered a PCE of 8.3%, with V_{oc} of 0.97 V, J_{sc} of 16.6 mA cm^{-2}, and FF of 0.52, while the best PbI_2:CsI = 2:1 solar cell yielded a PCE of 6.0%,

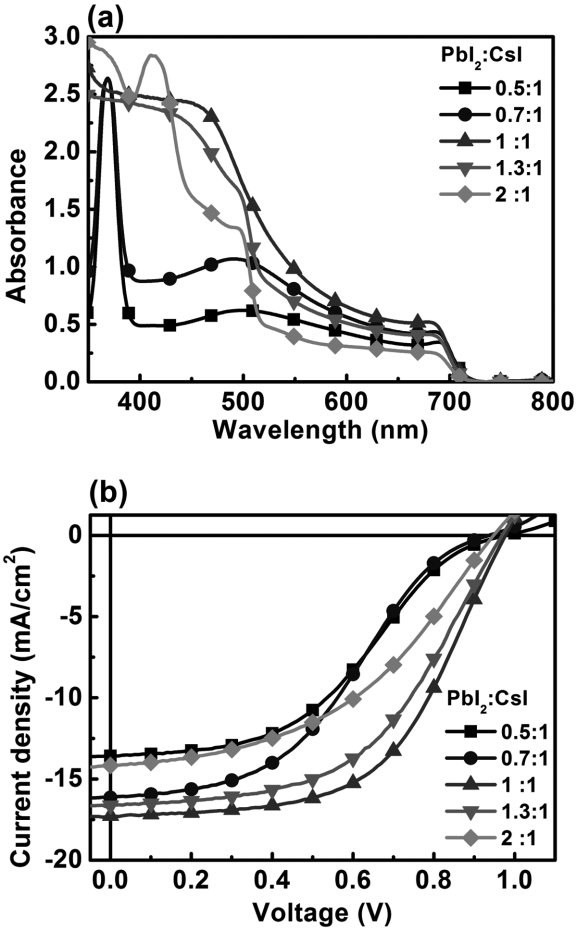

Figure 2. a) Absorption spectra of $CsPbI_3$ thin films with different PbI_2:CsI ratios after thermal annealing at 325 °C for 1 min. b) Corresponding *J–V* characteristics measured under 1 sun AM 1.5G illumination.

with V_{oc} of 0.95 V, J_{sc} of 14.2 mA cm^{-2}, and FF of 0.45. All CsI-rich solar cells exhibited a kink behavior. The best PbI_2:CsI = 0.7:1 solar cell showed a PCE of 6.0%, with V_{oc} of 0.94 V, J_{sc} of 16.1 mA cm^{-2}, and FF of 0.40, while the best PbI_2:CsI = 0.5:1 solar cell yielded a PCE of only 5.4%, with V_{oc} of 0.98 V, J_{sc} of 13.6 mA cm^{-2}, and FF of 0.41. Interestingly, the CsI-rich thin films exhibited strong absorption peaks at 370 nm, which corresponded to dips at the same wavelength in EQE spectra. Such strong absorption peaks could be attributed to the formation of Cs_4PbI_6.[23,24] Both thin-film absorption and device performance clearly indicated that the codeposition of stoichiometrically balanced precursors evidently provided the desired formation of $CsPbI_3$ along with higher device efficiency. An incorrect calibration of the CsI layer thickness can easily lead to unbalanced precursor molar ratio and significantly lower device efficiency; this may partially explain the high PCE value found here, which is more than twofold higher than that previously reported for vacuum codeposition of cesium lead halide.[15]

Snaith and co-workers showed that solution-processed mixed halide cesium-based perovskites presented better morphological stability than pure iodide $CsPbI_3$ perovskites.[16] Thus, we further explored vacuum-deposited mixed halide perovskites by codepositing stoichiometrically balanced PbI_2 and CsBr

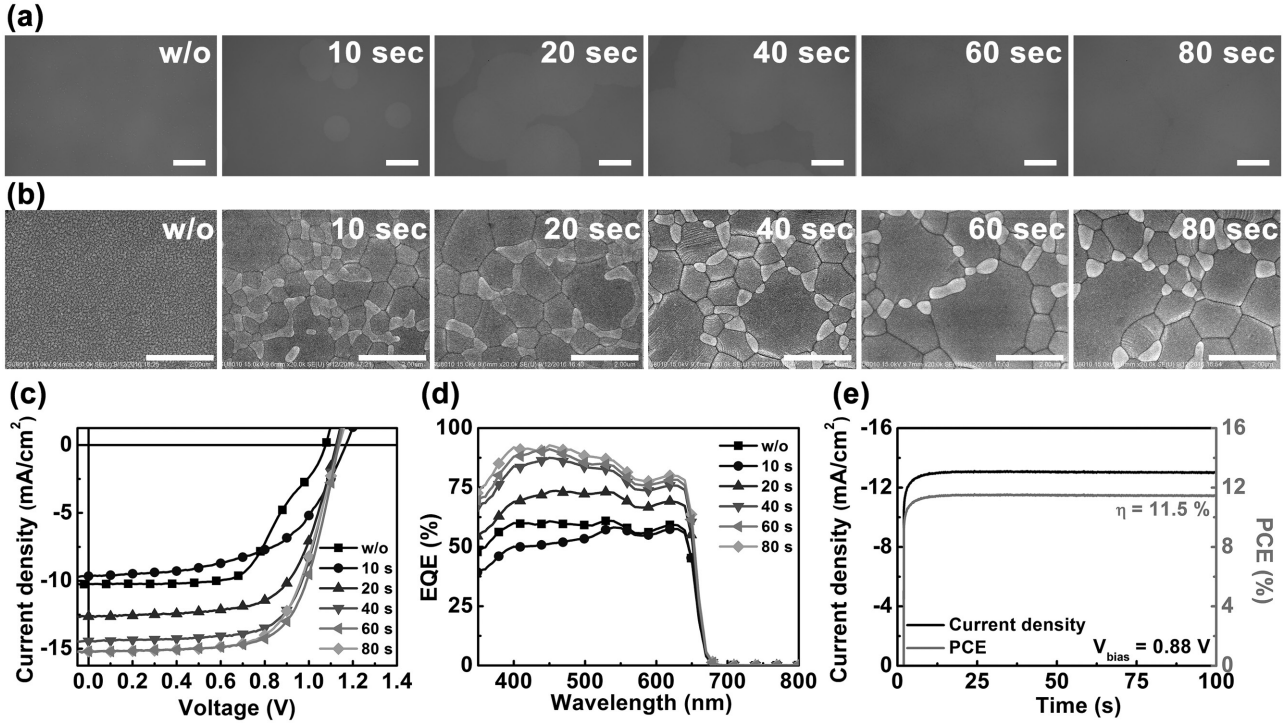

Figure 3. a) Optical microscopy images and b) top-view scanning electron microscopy images of $CsPbI_2Br$ thin films annealed for different times at 260 °C. Scale bar: a) 100 µm and b) 2 µm. c) Corresponding *J–V* characteristics and d) EQE spectra measured under 1 sun AM 1.5G illumination. e) Photocurrent density and power conversion efficiency as functions of time of the champion $CsPbI_2Br$ solar cell held at the bias of 0.88 V.

precursors. Notably, the as-deposited thin film already showed a dark-brownish appearance before postannealing. Optical and scanning electron microscopy (SEM) analyses performed on the postannealed film (260 °C) clearly revealed the film morphology evolution and color variation (**Figure 3**a,b). The as-deposited $CsPbI_2Br$ thin film exhibited substantially small crystalline domain size (≈100 nm). After annealing the sample for 60 s, the crystalline domains became as large as ≈3 µm. Contrast with organic perovskites, much higher postannealing temperature of 260 °C was required to obtain desired black phase in the $CsPbI_2Br$ active layer. However, only a short annealing time of ≈1 min was needed, which consumed much less energy compared with long-time, high-temperature sintering processes needed in the fabrication of the oxide carrier transport layers (e.g., TiO_2, NiO). The corresponding *J–V* characteristics, EQE spectra, and thin film absorption spectra are shown in Figure 3c,d, and Figure S2 in the Supporting Information, respectively. A shift in the absorption onset could be observed in mixed halide thin films. The optimized annealing time was 60 s, and the best device showed a very promising PCE of 11.8%, with high V_{oc} of 1.13 V, J_{sc} of 15.2 mA cm^{-2}, and FF of 0.68. Furthermore, unlike solution-processed cesium lead halide perovskite solar cells, whose stabilized efficiency was only about half of the *J–V* scan efficiency, the vacuum-deposited device showed a high stabilized efficiency of 11.5%, which was very close to the *J–V* scan efficiency (Figure 3e), as well as negligible hysteresis (Figure S3 and Table S1 in the Supporting Information). The performances of $CsPbI_3$ and $CsPbI_2Br$ solar cells are summarized in **Tables 1** and **2**.

To further investigate the $CsPbI_2Br$ thin film and device upon postannealing, grazing-incidence wide-angle X-ray scattering (GIWAXS) measurements were performed. The 2D GIWAXS patterns in **Figure 4**a–c revealed the structure and orientation evolutions of the film crystallites from the as-deposited state to the annealed state (10 and 60 s). The film crystallite orientation for the as-deposited and 10 s annealed films was mainly isotropic. The GIWAXS profile of the 10 s annealed film showed several peaks corresponding to the orthorhombic $CsPbI_3$ phase at room temperature, indicating that 10 s of annealing did not provide sufficient thermal energy to fully convert the low-temperature phase to the desired cubic perovskite phase.[25] The 60 s annealed sample, however, showed preferred orientation and well-ordered structure. Moreover, the GIWAXS profile derived from the 2D GIWAXS pattern of the 60 s annealed film (Figure 4d) was consistent with the calculated X-ray diffraction (XRD) data of cubic $CsPbI_3$ perovskite phase

Table 1. Performances of $CsPbI_3$ solar cells with different precursor ratios.

PbI_2:CsI	V_{OC} [V]	J_{SC} [mA cm^{-2}]	FF	PCE [%]
0.5:1	0.98 ± 0.01	14.0 ± 0.4	0.38 ± 0.05	5.3 ± 0.2 (5.4)
0.7:1	0.94 ± 0.01	16.1 ± 0.1	0.38 ± 0.01	5.7 ± 0.2 (6.0)
1:1	0.97 ± 0.01	17.4 ± 0.1	0.56 ± 0.01	9.1 ± 0.2 (9.4)
1.3:1	0.96 ± 0.02	16.5 ± 0.1	0.51 ± 0.01	8.1 ± 0.2 (8.3)
2:1	0.94 ± 0.01	14.3 ± 0.1	0.43 ± 0.02	5.8 ± 0.2 (6.0)

Table 2. Performances of $CsPbI_2Br$ solar cells annealed at 260 °C for different times.

Annealing	V_{OC} [V]	J_{SC} [mA cm^{-2}]	FF	PCE [%]
w/o	1.10 ± 0.02	10.7 ± 0.4	0.59 ± 0.02	6.8 ± 0.2 (6.9)
10 s	1.16 ± 0.02	9.0 ± 0.5	0.58 ± 0.01	6.0 ± 0.2 (6.3)
20 s	1.13 ± 0.01	12.5 ± 0.4	0.63 ± 0.03	9.0 ± 0.2 (9.3)
40 s	1.13 ± 0.01	14.3 ± 0.2	0.60 ± 0.03	11.0 ± 0.1 (11.1)
60 s	1.15 ± 0.02	15.2 ± 0.3	0.67 ± 0.01	11.7 ± 0.1 (11.8)
80 s	1.13 ± 0.02	15.2 ± 0.1	0.66 ± 0.01	11.2 ± 0.1 (11.3)

at high temperature, with diffraction peaks at scattering vectors Q ($Q = 4\pi/\lambda \cdot \sin\theta$, where θ corresponds to the diffraction angle) of ≈10, 14.2, 20, and 28.5 nm^{-1}.[25] The peak with the highest intensity (200) was at Q = 20 nm^{-1}. The measured GIWAXS profile was slightly different from the calculated XRD of cubic $CsPbI_3$ perovskite phase, owing to the effect of bromide content on the lattice.

As the phase transition temperature of cesium lead halide perovskites is significantly higher than that of organic lead halides, other literature has already reported the superior stability of cesium lead halides at high temperature.[18,22,26] Here, we found a very interesting preliminary result; as shown in **Figure 5**, the vacuum-deposited $CsPbI_2Br$ solar cell showed better long-term stability than the organic lead halide counterpart with the same HTL and ETL structure. The device maintained 96% of its peak efficiency after more than 2 months. The continuous light soaking test, as shown in Figure S4 in the Supporting Information, also revealed a stable performance of vacuum-deposited $CsPbI_2Br$ solar cells under a high excitation light intensity. Surprisingly, the vacuum-deposited $CsPbI_3$ did not exhibit the same stability. The $CsPbI_3$ film quickly degraded, assuming a transparent appearance (yellow phase) after 2 weeks, even with an encapsulation (see the inset in Figure 5). The thermal stability and phase transition of the vacuum deposited $CsPbI_2Br$ and $CsPbI_3$ thin films were further studied. As shown in Figure S5 in the Supporting Information, the $CsPbI_2Br$ films exhibited much better thermal stability and maintained black phase upon 120 °C annealing. In contrast, the $CsPbI_3$ thin films soon went back to the yellow phase at a much lower heating temperature of 80 °C. By reheating the yellow phase of the $CsPbI_3$ thin films, the films turned back into black appearances. These results, together with the appearances of the devices stored at room temperature for 2 weeks, indicate that the $CsPbI_3$ is only temporarily in the black phase and tends to go back to the room temperature stable yellow phase. However, the $CsPbI_2Br$ films are very stable in their black phase at both room temperature and the elevated temperature up to 120 °C.

Very recently, Luther and co-workers also reported inorganic perovskite solar cells with PCE of 10.77% based on passivated $CsPbI_3$ quantum dots.[27] Although the current 11–12% PCE of the best all-inorganic cesium lead halide perovskite solar cells still lag much behind 20–22% PCE of perovskites with either organic cations or mixed inorganic–organic cations, there is no decided reason for an all-inorganic perovskite to show an inferior efficiency.[28–33] The mismatched E_g of $CsPbI_2Br$ for solar light harvesting can be tuned smaller by incorporation of tin cations or lower the ratio of bromides.[16,34–37] More complex mixed cations (e.g., RbCs) perovskites and double perovskites (e.g., Cs_2AgBiI_6) may further open up the tunability of E_g, optoelectronic properties, and thin-film morphologies.[29,38–40] They are all feasible by the vacuum deposition. However, a precise deposition of multiple evaporation sources could be quite challenging.

The large E_g of $CsPbI_2Br$ and high V_{oc} of the devices suggested that the devices are quite suitable for dim-light energy harvesting. Figure S6 in the Supporting Information shows the J–V characteristics of the $CsPbI_2Br$ cell under fluorescent light illumination. The performances of all the devices are summarized in Table S2 in the Supporting Information. Although

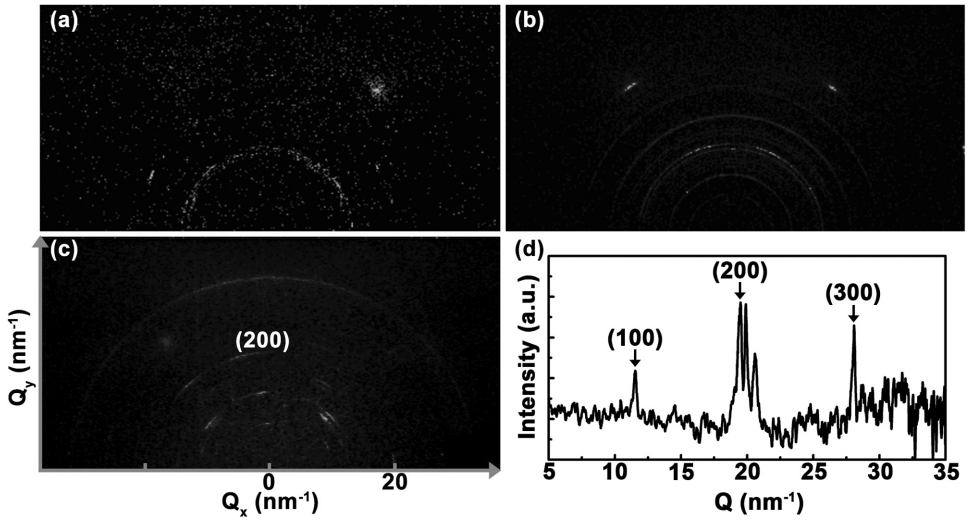

Figure 4. 2D grazing-incidence wide-angle X-ray scattering (GIWAXS) patterns of a) as-deposited film and films annealed for b) 10 s and c) 60 s. d) The GIWAXS profile derived from the azimuthal ring average of (c). Q_x is along the in-plane direction (parallel to the film surface), while Q_y is along the out-of-plane direction (normal to the film surface).

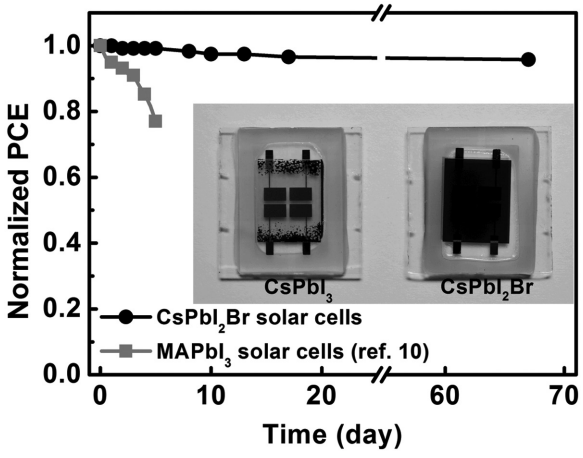

Figure 5. Long-term PCE stability of the champion $CsPbI_2Br$ solar cell and vacuum-deposited $MAPbI_3$ perovskite solar cell stored in the dark with encapsulations.[10] The initial PCEs of the $CsPbI_2Br$ and the $MAPbI_3$ perovskite solar cells were 11.8 and 17.6%, respectively. Inset: photographs of $CsPbI_3$ (left) and $CsPbI_2Br$ (right) perovskite solar cells after 2 weeks.

the efficiency of the $CsPbI_2Br$ solar cell under 1 sun illumination still lagged largely behind the efficiency of state-of-the-art organic lead halide solar cells, the PCE of 26.6% at 1000 lux was already 97% of the best PCE value reported for organic lead halide under similar dim-light conditions.[3] The results can be explained by considering the larger V_{oc} and excellent match of the $CsPbI_2Br$ absorption spectrum with the spectral distribution of the artificial light. We believe that, upon further optimization, PCEs exceeding 30% can be achieved.

In summary, upon replacing organic halides with cesium halides, a common vacuum codeposition technique was used to fabricate perovskite thin films and solar cells. Highly precise cesium halide thin-film thickness and calibration tooling factor were obtained by protecting the films against air exposure throughout deposition and measurement. The accurate control of the stoichiometric ratios of the precursors was found to be critical for device performance. By incorporating vacuum-deposited ETLs and HTLs, efficient all-vacuum-deposited cesium-based perovskite solar cells were fabricated. The stoichiometrically balanced $CsPbI_3$ solar cell delivered the highest PCE of 9.4%. After introducing bromide content, the PCE of the $CsPbI_2Br$ device was further boosted to 11.8%, with high V_{OC} of 1.13 V, J_{SC} of 15.2 mA cm^{-2}, and FF of 0.68. The $CsPbI_2Br$ device also showed a promising stabilized PCE of 11.5%, which was very close to the *J–V* scan efficiency. Mixed halide devices also showed small hystereses and superior stabilities. In addition, the good match of the mixed halide device absorption spectrum with the artificial light spectrum and the promising preliminary PCE of 26.6% under 1000 lux fluorescent light illumination favor the use of these devices for dim-light energy harvesting. The results provide a paragon for the use of inorganic precursors en route to efficient vacuum-deposited perovskite devices.

Experimental Section

Tooling Factor Calibration: The tooling factor was initially set to 1 in the thickness monitor program. The correct tooling factor was calculated as follows: $F_m = T_m/T_i$, where T_i was the film thickness indicated by the quartz crystal microbalance sensor and T_m was the actual film thickness measured with a J. A. Woollam V-VASE ellipsometer. Silicon wafers with area of 2×2 cm^2 with native oxide (≈2 nm) were used as the substrates in the ellipsometry measurements. The measurements were performed over the wavelength range of 400–1100 nm in steps of 10 nm. For the PbI_2 thin films, the angles of light incidence were between 55° and 75° relative to the surface normal in steps of 10°. The analysis of the ellipsometric data was performed using the software WVASE32 (J. A. Woollam Co.). The thickness of the PbI_2 thin film was determined by assuming that n obeyed the Cauchy equation and that $k = 0$ in the wavelength range of 700–1100 nm (transparent region). For cesium halide thin films, the as-deposited samples were transferred to a nitrogen-filled glove box, and then loaded into a custom-made ellipsometry vacuum stage with observation and measurement windows. Subsequently, the stage was pumped down to ≈10^{-3} torr by a mechanical pump in the glove box, and then transferred to the ellipsometer. The cesium halide thin films were kept under ≈10^{-3} torr vacuum throughout the transportation and measurement. The stage chamber was carefully designed so that, during the ellipsometry measurement, the incident and reflected lights were normally incident on the measurement windows. The angle of incident light was set at 70° relative to the surface normal. The thickness of the cesium halide thin film was determined by assuming that n obeyed the Cauchy equation and that $k = 0$ in the wavelength range of 450–1100 nm (transparent region). The calibrated tooling factors were then subsequently applied during codeposition. The molar ratios of the precursors were calculated from the calibrated film thicknesses, molecular weights of each species, and densities of PbI_2, CsI, and CsBr (6.16, 4.51, and 4.44 g cm^{-3}, respectively) as found in the literature.

Device Preparation: Small organic molecules were purified once by temperature-gradient sublimation before use. Precleared ITO-coated glasses were used as substrates. The substrates were loaded into a high-vacuum chamber (base pressure ≈2×10^{-6} torr) to deposit Ca, C_{60}, and perovskite layer-by-layer. The substrates were kept at room temperature with the sample holder rotating at 30 rpm. For perovskite layers with PbI_2:CsI molar ratios of 2:1, 1.3:1, 1:1, 0.7:1, and 0.5:1, PbI_2 was deposited at the rate of 0.91 Å s^{-1}, while CsI was deposited at the rates of 0.35, 0.54, 0.7, 1, and 1.4 Å s^{-1}, respectively. The deposition rate for PbI_2, CsI, and CsBr typically varied in the range of ±5% during the codeposition process. During codeposition, the deposition rate was monitored by three quartz crystal microbalance sensors; the first sensor monitored the deposition rate of lead halide, the second monitored the deposition rate of cesium halides, and the third monitored the total deposition rate on the sample. The samples were annealed at 325 °C for 1 min in anhydrous nitrogen atmosphere to obtain the desired dark-brownish appearance. For $CsPbI_2Br$ thin films and devices, PbI_2 and CsBr were deposited at the rates of 0.78 and 0.5 Å s^{-1}, respectively. Then, the samples were annealed at 260 °C in anhydrous nitrogen atmosphere. After thermal annealing, the samples were transferred back to the high-vacuum chamber for 4,4′-cyclohexylidenebis[*N,N* -bis(4-methylphenyl)benzenamine] (TAPC), TAPC:MoO_3 (65:35, v/v), MoO_3, and Ag depositions. The devices were configured as glass substrate/ITO (145 nm)/Ca (1 nm)/C_{60} (5 nm)/$CsPbI_3$ (300 nm) or $CsPbI_2Br$ (400 nm)/TAPC (10 nm)/TAPC:MoO_3 (160 nm)/Ag (150 nm). The device areas (0.051 cm^2) were defined by shadow masks. The devices were encapsulated using ultraviolet (UV) cured sealant (Everwide Chemical Co.) and cover glasses after fabrication, and subsequently characterized in air.

Characterization: SEM images were obtained using a Hitachi SU8010 field-emission scanning electron microscope. ITO/Ca/C_{60} coated glasses were used as substrates. The thicknesses of ITO, Ca, and C_{60} were 145, 1, and 5 nm, respectively. The samples for the SEM measurements were prepared using the same conditions as those used for the device fabrication. The samples were transferred to a vacuum chamber and quickly loaded into the SEM antechamber to reduce the air exposure time down to ≈10 s. For the GIWAXS measurements, film specimens with area of 2×2 cm^2 were deposited on Ca/C_{60}-coated Si substrates.

The thicknesses of the Ca and C_{60} films were 1 and 5 nm, respectively. The samples were quickly loaded into the GIWAXS instrument to reduce the air exposure time to ≈30 s. The GIWAXS experiments were conducted with collection time of 30 min by using a Bruker instrument (AXS GmbH, Nanostar) operated at 2.5 kW (50 kV, 50 mA) and room temperature in vacuum. The GIWAXS instrument possessed a well-collimated system and a 2D image plate detector with an area of 20×25 cm^2. The standard sample for calibration was silver behenate powder. The absorption spectra were acquired using a Shimadzu UV-2600 spectrophotometer; here, the samples were encapsulated by using UV-cured sealant and cover glasses. The J–V characteristics of the devices were measured using a Keithley 2636B SourceMeter in the dark, under AM 1.5G simulated solar illumination with an intensity of 100 mW cm^{-2} (1 sun, calibrated by an NREL-traceable KG5 filtered silicon reference cell), and under 6500 K color temperature Philips T5 fluorescent lamp illumination. The irradiance and luminance of the T5 fluorescent lamp were determined using NIST-traceable Ophir radiometer (PD300-BB-50 mW) and photometer (PD300-CIE), respectively. Normally, the scan direction was from positive to negative bias, with a step size of 10 mV and a delay time between points of 300 ms. The EQE spectra were taken by illuminating the solar cells with chopped monochromatic light with a continuous-wave bias white light (from a halogen lamp). The photocurrent signals were extracted with lock-in technique using a Stanford Research System current preamplifier followed by an Ametek lock-in amplifier. The intensity of the monochromatic light was calibrated with an NIST-traceable Ophir power meter. The device stability test was performed with UV-epoxy encapsulated cells. The cells were stored in dark environment at room temperature (≈25 °C) and regularly measured under an AM 1.5G, 1 sun, simulated solar illumination. The J–V sweeping direction was from positive to negative bias, with a step size of 10 mV and a delay time between points of 300 ms. The light soaking test was performed with UV-epoxy encapsulated cells. The cells were continuously illuminated with an ≈100 mW cm^{-2} white light from a filtered halogen lamp under ambient conditions. An ≈1 kΩ load was applied with the cell while under illumination. The devices were regularly taken out from the light soaking chamber and measured with an AM 1.5G, 1 sun, solar simulator. The J–V sweeping direction was from positive to negative bias, with a step size of 10 mV and a delay time between points of 300 ms.

Supporting Information

Supporting Information is available from the Wiley Online Library or from the author.

Acknowledgements

The authors would like to acknowledge the financial support from the Ministry of Science and Technology of Taiwan, National Tsing Hua University, and Institute of Nuclear Energy Research.

Received: September 30, 2016
Revised: November 14, 2016
Published online: January 20, 2017

[1] A. Kojima, K. Teshima, Y. Shirai, T. Miyasaka, *J. Am. Chem. Soc.* **2009**, *131*, 6050.
[2] H.-S. Kim, C.-R. Lee, J.-H. Im, K.-B. Lee, T. Moehl, A. Marchioro, S.-J. Moon, R. Humphry-Baker, J.-H. Yum, J. E. Moser, M. Grätzel, N.-G. Park, *Sci. Rep.* **2012**, *2*, 591.
[3] C.-Y. Chen, J.-H. Chang, K.-M. Chiang, H.-L. Lin, S.-Y. Hsiao, H.-W. Lin, *Adv. Funct. Mater.* **2015**, *25*, 7064.
[4] Z.-K. Tan, R. S. Moghaddam, M. L. Lai, P. Docampo, R. Higler, F. Deschler, M. Price, A. Sadhanala, L. M. Pazos, D. Credgington, F. Hanusch, T. Bein, H. J. Snaith, R. H. Friend, *Nat. Nanotechnol.* **2014**, *9*, 687.
[5] H. Cho, S.-H. Jeong, M.-H. Park, Y.-H. Kim, C. Wolf, C.-L. Lee, J. H. Heo, A. Sadhanala, N. Myoung, S. Yoo, S. H. Im, R. H. Friend, T.-W. Lee, *Science* **2015**, *350*, 1222.
[6] H. Zhu, Y. Fu, F. Meng, X. Wu, Z. Gong, Q. Ding, M. V. Gustafsson, M. T. Trinh, S. Jin, X. Y. Zhu, *Nat. Mater.* **2015**, *14*, 636.
[7] M. Liu, M. B. Johnston, H. J. Snaith, *Nature* **2013**, *501*, 395.
[8] C.-W. Chen, H.-W. Kang, S.-Y. Hsiao, P.-F. Yang, K.-M. Chiang, H.-W. Lin, *Adv. Mater.* **2014**, *26*, 6647.
[9] L. K. Ono, S. Wang, Y. Kato, S. R. Raga, Y. Qi, *Energy Environ. Sci.* **2014**, *7*, 3989.
[10] S.-Y. Hsiao, H.-L. Lin, W.-H. Lee, W.-L. Tsai, K.-M. Chiang, W.-Y. Liao, C.-Z. Ren-Wu, C.-Y. Chen, H.-W. Lin, *Adv. Mater.* **2016**, *28*, 7013.
[11] J. Gong, S. B. Darling, F. You, *Energy Environ. Sci.* **2015**, *8*, 1953.
[12] M. R. Leyden, L. K. Ono, S. R. Raga, Y. Kato, S. Wang, Y. Qi, *J. Mater. Chem. A* **2014**, *2*, 18742.
[13] M. R. Leyden, Y. Jiang, Y. Qi, *J. Mater. Chem. A* **2016**, *4*, 13125.
[14] M. M. Tavakoli, L. Gu, Y. Gao, C. Reckmeier, J. He, A. L. Rogach, Y. Yao, Z. Fan, *Sci. Rep.* **2015**, *5*, 14083.
[15] Q. Ma, S. Huang, X. Wen, M. A. Green, A. W. Y. Ho-Baillie, *Adv. Energy Mater.* **2016**, *6*, 1502202.
[16] R. J. Sutton, G. E. Eperon, L. Miranda, E. S. Parrott, B. A. Kamino, J. B. Patel, M. T. Hörantner, M. B. Johnston, A. A. Haghighirad, D. T. Moore, H. J. Snaith, *Adv. Energy Mater.* **2016**, *6*, 1502458.
[17] C. F. J. Lau, X. Deng, Q. Ma, J. Zheng, J. S. Yun, M. A. Green, S. Huang, A. W. Y. Ho-Baillie, *ACS Energy Lett.* **2016**, *1*, 573.
[18] R. E. Beal, D. J. Slotcavage, T. Leijtens, A. R. Bowring, R. A. Belisle, W. H. Nguyen, G. F. Burkhard, E. T. Hoke, M. D. McGehee, *J. Phys. Chem. Lett.* **2016**, *7*, 746.
[19] G. E. Jabbour, B. Kippelen, N. R. Armstrong, N. Peyghambarian, *Appl. Phys. Lett.* **1998**, *73*, 1185.
[20] K. Zenken, Y. Kazuo, K. Hirotake, H. Kohtaku, O. Yutaka, *Jpn. J. Appl. Phys.* **2006**, *45*, 3737.
[21] R. Zheng, W. Huang, W. Xu, Y. Cao, *Synth. Met.* **2012**, *162*, 1919.
[22] C. C. Stoumpos, C. D. Malliakas, M. G. Kanatzidis, *Inorg. Chem.* **2013**, *52*, 9019.
[23] S. Kondo, A. Masaki, T. Saito, H. Asada, *Solid State Commun.* **2002**, *124*, 211.
[24] F. Somma, M. Nikl, K. Nitsch, C. Giampaolo, A. R. Phani, S. Santucci, *Thin Solid Films* **2000**, *373*, 195.
[25] D. M. Trots, S. V. Myagkota, *J. Phys. Chem. Solids* **2008**, *69*, 2520.
[26] C. K. Moller, *Nature* **1958**, *182*, 1436.
[27] A. Swarnkar, A. R. Marshall, E. M. Sanehira, B. D. Chernomordik, D. T. Moore, J. A. Christians, T. Chakrabarti, J. M. Luther, *Science* **2016**, *354*, 92.
[28] D. Bi, C. Yi, J. Luo, J.-D. Décoppet, F. Zhang, S. M. Zakeeruddin, X. Li, A. Hagfeldt, M. Grätzel, *Nat. Energy* **2016**, *1*, 16142.
[29] M. Saliba, T. Matsui, K. Domanski, J.-Y. Seo, A. Ummadisingu, S. M. Zakeeruddin, J.-P. Correa-Baena, W. R. Tress, A. Abate, A. Hagfeldt, M. Grätzel, *Science* **2016**, *354*, 206.
[30] M. Saliba, T. Matsui, J.-Y. Seo, K. Domanski, J.-P. Correa-Baena, M. K. Nazeeruddin, S. M. Zakeeruddin, W. Tress, A. Abate, A. Hagfeldt, M. Grätzel, *Energy Environ. Sci.* **2016**, *9*, 1989.
[31] X. Li, D. Bi, C. Yi, J.-D. Décoppet, J. Luo, S. M. Zakeeruddin, A. Hagfeldt, M. Grätzel, *Science* **2016**, *353*, 58.
[32] Y. C. Kim, N. J. Jeon, J. H. Noh, W. S. Yang, J. Seo, J. S. Yun, A. Ho-Baillie, S. Huang, M. A. Green, J. Seidel, T. K. Ahn, S. I. Seok, *Adv. Energy Mater.* **2016**, *6*, 1502104.
[33] W. S. Yang, J. H. Noh, N. J. Jeon, Y. C. Kim, S. Ryu, J. Seo, S. I. Seok, *Science* **2015**, *348*, 1234.
[34] Y. Li, W. Sun, W. Yan, S. Ye, H. Rao, H. Peng, Z. Zhao, Z. Bian, Z. Liu, H. Zhou, C. Huang, *Adv. Energy Mater.* **2016**, *6*, 1601353.

[35] F. Zuo, S. T. Williams, P.-W. Liang, C.-C. Chueh, C.-Y. Liao, A. K. Y. Jen, *Adv. Mater.* **2014**, *26*, 6454.
[36] F. Hao, C. C. Stoumpos, R. P. H. Chang, M. G. Kanatzidis, *J. Am. Chem. Soc.* **2014**, *136*, 8094.
[37] Y. Ogomi, A. Morita, S. Tsukamoto, T. Saitho, N. Fujikawa, Q. Shen, T. Toyoda, K. Yoshino, S. S. Pandey, T. Ma, S. Hayase, *J. Phys. Chem. Lett.* **2014**, *5*, 1004.
[38] G. Volonakis, M. R. Filip, A. A. Haghighirad, N. Sakai, B. Wenger, H. J. Snaith, F. Giustino, *J. Phys. Chem. Lett.* **2016**, *7*, 1254.
[39] M. R. Filip, S. Hillman, A. A. Haghighirad, H. J. Snaith, F. Giustino, *J. Phys. Chem. Lett.* **2016**, *7*, 2579.
[40] A. H. Slavney, T. Hu, A. M. Lindenberg, H. I. Karunadasa, *J. Am. Chem. Soc.* **2016**, *138*, 2138.